



# Imaging the 44 au Kuiper Belt Analog Debris Ring around HD 141569A with GPI Polarimetry

Juan Sebastián Bruzzone<sup>1</sup> , Stanimir Metchev<sup>1,2,3</sup> , Gaspard Duchêne<sup>4,5</sup> , Maxwell A. Millar-Blanchaer<sup>6</sup>, Ruobing Dong<sup>7</sup> , Thomas M. Esposito<sup>4</sup> , Jason J. Wang<sup>4</sup> , James R. Graham<sup>4</sup>, Johan Mazoyer<sup>6</sup> , Schuyler Wolff<sup>8</sup> , S. Mark Ammons<sup>9</sup> , Adam C. Schneider<sup>10</sup> , Alexandra Z. Greenbaum<sup>11</sup> , Brenda C. Matthews<sup>7,12</sup> , Pauline Arriaga<sup>13</sup> , Vanessa P. Bailey<sup>6</sup> , Travis Barman<sup>14</sup> , Joanna Bulger<sup>15</sup> , Jeffrey Chilcote<sup>16,17</sup> , Tara Cotten<sup>18</sup> , Robert J. De Rosa<sup>4</sup> , Rene Doyon<sup>19</sup>, Michael P. Fitzgerald<sup>13</sup> , Katherine B. Follette<sup>20</sup> , Benjamin L. Gerard<sup>7,12</sup> , Stephen J. Goodsell<sup>21</sup> , Pascale Higon<sup>22</sup> , Justin Hom<sup>10</sup> , Li-Wei Hung<sup>13</sup> , Patrick Ingraham<sup>23</sup> , Paul Kalas<sup>4,24</sup>, Quinn Konopacky<sup>25</sup> , James E. Larkin<sup>13</sup> , Bruce Macintosh<sup>16</sup> , Jérôme Maire<sup>25</sup>, Franck Marchis<sup>24</sup> , Christian Marois<sup>7,12</sup> , Katie M. Morzinski<sup>26</sup> , Eric L. Nielsen<sup>16,24</sup> , Rebecca Oppenheimer<sup>27</sup> , David Palmer<sup>9</sup> , Rahul Patel<sup>28</sup> , Jennifer Patience<sup>10</sup>, Marshall Perrin<sup>8</sup> , Lisa Poyneer<sup>9</sup>, Laurent Pueyo<sup>8</sup>, Abhijith Rajan<sup>10</sup> , Julien Rameau<sup>19</sup> , Fredrik T. Rantakyro<sup>29</sup> , Dmitry Savransky<sup>30</sup> , Anand Sivaramakrishnan<sup>8</sup> , Inseok Song<sup>18</sup> , Remi Soumer<sup>8</sup> , Sandrine Thomas<sup>23</sup> , J. Kent Wallace<sup>6</sup>, Kimberly Ward-Duong<sup>20</sup> , and Sloane Wiktorowicz<sup>31</sup>

<sup>1</sup> Department of Physics and Astronomy, The University of Western Ontario, London, ON N6A 3K7, Canada

<sup>2</sup> Institute of Earth and Space Exploration, London, ON N6A 3K7, Canada; [smetchev@uwo.ca](mailto:smetchev@uwo.ca)

<sup>3</sup> Department of Physics & Astronomy, Stony Brook University, Stony Brook, NY 11794-3800, USA

<sup>4</sup> Astronomy Department, University of California, Berkeley, CA 94720, USA

<sup>5</sup> Université Grenoble Alpes, CNRS, IPAG, Grenoble, F-38000, France

<sup>6</sup> Jet Propulsion Laboratory, California Institute of Technology, Pasadena, CA 91109, USA

<sup>7</sup> University of Victoria, 3800 Finnerty Road, Victoria, BC V8P 5C2, Canada

<sup>8</sup> Space Telescope Science Institute, Baltimore, MD 21218, USA

<sup>9</sup> Lawrence Livermore National Laboratory, Livermore, CA 94551, USA

<sup>10</sup> School of Earth and Space Exploration, Arizona State University, P.O. Box 871404, Tempe, AZ 85287, USA

<sup>11</sup> Department of Astronomy, University of Michigan, Ann Arbor, MI 48109, USA

<sup>12</sup> National Research Council of Canada Herzberg, 5071 West Saanich Road, Victoria, BC V9E 2E7, Canada

<sup>13</sup> Department of Physics & Astronomy, University of California, Los Angeles, CA 90095, USA

<sup>14</sup> Lunar and Planetary Laboratory, University of Arizona, Tucson, AZ 85721, USA

<sup>15</sup> Subaru Telescope, NAOJ, 650 North A'ohoku Place, Hilo, HI 96720, USA

<sup>16</sup> Kavli Institute for Particle Astrophysics and Cosmology, Stanford University, Stanford, CA 94305, USA

<sup>17</sup> Department of Physics, University of Notre Dame, 225 Nieuwland Science Hall, Notre Dame, IN 46556, USA

<sup>18</sup> Department of Physics and Astronomy, University of Georgia, Athens, GA 30602, USA

<sup>19</sup> Institut de Recherche sur les Exoplanètes, Département de Physique, Université de Montréal, Montréal, QC H3C 3J7, Canada

<sup>20</sup> Physics and Astronomy Department, Amherst College, 21 Merrill Science Drive, Amherst, MA 01002, USA

<sup>21</sup> Gemini Observatory, 670 North A'ohoku Place, Hilo, HI 96720, USA

<sup>22</sup> European Southern Observatory, 3107 Alonso de Córdova, Vitacura, Santiago, Chile

<sup>23</sup> Large Synoptic Survey Telescope, 950 North Cherry Avenue, Tucson, AZ 85719, USA

<sup>24</sup> SETI Institute, Carl Sagan Center, 189 Bernardo Avenue, Mountain View, CA 94043, USA

<sup>25</sup> Center for Astrophysics and Space Science, University of California San Diego, La Jolla, CA 92093, USA

<sup>26</sup> Steward Observatory, University of Arizona, Tucson, AZ 85721, USA

<sup>27</sup> Department of Astrophysics, American Museum of Natural History, New York, NY 10024, USA

<sup>28</sup> Infrared Processing and Analysis Center, California Institute of Technology, Pasadena, CA 91125, USA

<sup>29</sup> Gemini Observatory, Casilla 603, La Serena, Chile

<sup>30</sup> Sibley School of Mechanical and Aerospace Engineering, Cornell University, Ithaca, NY 14853, USA

<sup>31</sup> Department of Astronomy, UC Santa Cruz, 1156 High Street, Santa Cruz, CA 95064, USA

Received 2018 May 11; revised 2019 November 25; accepted 2019 November 26; published 2020 January 16

## Abstract

We present the first polarimetric detection of the inner disk component around the pre-main-sequence B9.5 star HD 141569A. Gemini Planet Imager *H*-band (1.65  $\mu\text{m}$ ) polarimetric differential imaging reveals the highest signal-to-noise ratio detection of this ring yet attained and traces structure inward to  $0''.25$  (28 au at a distance of 111 pc). The radial polarized intensity image shows the east side of the disk, peaking in intensity at  $0''.40$  (44 au) and extending out to  $0''.9$  (100 au). There is a spiral arm-like enhancement to the south, reminiscent of the known spiral structures on the outer rings of the disk. The location of the spiral arm is coincident with  $^{12}\text{CO } J = 3-2$  emission detected by ALMA and hints at a dynamically active inner circumstellar region. Our observations also show a portion of the middle dusty ring at  $\sim 220$  au known from previous observations of this system. We fit the polarized *H*-band emission with a continuum radiative transfer Mie model. Our best-fit model favors an optically thin disk with a minimum dust grain size close to the blowout size for this system, evidence of ongoing dust production in the inner reaches of the disk. The thermal emission from this model accounts for virtually all of the far-infrared and millimeter flux from the entire HD 141569A disk, in agreement with the lack of ALMA continuum and CO emission beyond  $\sim 100$  au. A remaining 8–30  $\mu\text{m}$  thermal excess a factor of  $\sim 2$  above our model argues for an as-yet-unresolved warm innermost 5–15 au component of the disk.

*Unified Astronomy Thesaurus concepts:* Debris disks (363); Circumstellar disks (235); Polarimetry (1278); Astronomical techniques (1684); Coronagraphic imaging (313); Direct imaging (387)

## 1. Introduction

Debris disks are established laboratories to study planet formation and evolution. Planetesimals and infant planets interact with the dusty disk and create gaps, asymmetries, offsets, and local enhancements through various dynamical mechanisms that help infer their presence (e.g., the  $\beta$  Pictoris disk and planet; Lagage & Pantin 1994; Kalas & Jewitt 1995; Lagrange et al. 2010). Of special interest are those young disks (up to 40 Myr) transitioning between the protoplanetary disk and debris disk stage. These “hybrid disks” contain gas that can be either primordial or secondary (e.g., Moór et al. 2017) and often show a significant deficit in near- or mid-IR emission or an inner clearing in resolved images (e.g., HD 163296, Doucet et al. 2006; 49 Ceti, Hughes et al. 2008; HD 21997, Kóspál et al. 2013). The study of hybrid disks is attractive because of the implications for gas giant planet formation and gas–dust interaction models in nascent planetary systems.

The star HD 141569A ( $V = 7.12$  mag, Høg et al. 2000;  $H = 6.86$  mag, Cutri et al. 2003) is a well-known hybrid disk host. A young  $5 \pm 3$  Myr (Weinberger et al. 2000) B9.5V star (Jaschek & Jaschek 1992), HD 141569A is at a distance of  $110.5 \pm 0.5$  pc (Gaia Collaboration et al. 2018) with  $L_{\text{IR}}/L_{\text{star}} \sim 8 \times 10^{-3}$  (Sylvester et al. 1996) and two low-mass stellar companions, B and C, at roughly  $9''$  (Weinberger et al. 2000). Early 12–100  $\mu\text{m}$  photometry with *IRAS* indicated a population of  $\sim 100$  K circumstellar dust at an estimated distance of 47–60 au (Jaschek et al. 1986; Walker & Wolstencroft 1988).

The first high-contrast coronagraphic images in scattered light with the *Hubble Space Telescope* (*HST*)/NICMOS at  $\sim 1.6\mu\text{m}$  (F160W) revealed a bright dusty disk inclined at  $53^\circ \pm 5^\circ$  and a position angle (PA) of  $355^\circ \pm 1^\circ$  (Augereau et al. 1999a; Weinberger et al. 1999). Weinberger et al. (1999) reported a disk extending out to  $4''$  with two conspicuous nested rings peaking at  $2''.0$  (220 au) and  $3''.3$  (360 au; along the semimajor axis of the disk), separated by a  $1''$  wide gap devoid of scattering material. In this work, we refer to the 220 and 360 au rings as the middle and outer rings, respectively. The brighter eastern side of the system is likely nearer to us under the assumption of preferentially forward scattering by dust (Weinberger et al. 1999). Subsequently, *HST* optical coronagraphic observations with the Space Telescope Imaging Spectrograph (STIS; 365–806  $\mu\text{m}$ , 50 CCD; Mouillet et al. 2001) and Advanced Camera for Surveys (ACS) at 430 nm (F435W), 590 nm (F606W), and 830 nm (F814W; Clampin et al. 2003) revealed asymmetries and two prominent tightly wound spiral substructures: an inner arm between  $1''.8$  and  $2''.2$  (200 and 240 au) and an outer broad ring at  $3''.0$ – $4''.0$  (330–440 au). In a new analysis of archival Gemini/NICI and *HST*/NICMOS data, Mazoyer et al. (2016) reported a split in two fine rings in the eastern part of the disk and showed that the  $2''$  ring shows a small  $0''.03$  offset relative to the central star.

Marsh et al. (2002) were the first to suggest a peak in the dust optical depth inward of  $\sim 70$  au from mid-IR imaging with Keck/MIRLIN (Ressler et al. 1994). High-contrast coronagraphic observations in the near-IR with the Very Large Telescope (VLT)/SPHERE further revealed the presence of a third inner ring at  $\sim 44$  au (Perrot et al. 2016). This resolved inner disk component was also seen as an arc-like rim by Konishi et al. (2016) in optical broadband light with *HST*/STIS and marginally detected by Currie et al. (2016) with Keck/NIRC2 at  $L_p$ . Mawet et al. (2017)

confirmed the detection of the inner disk component around HD 141569A in  $L_p$ -band scattered light with a vortex coronagraph in Keck/NIRC2. The combination of optical/near-IR scattered light and 870  $\mu\text{m}$ /2.9 mm Atacama Large Millimeter/submillimeter Array (ALMA) observations (White et al. 2016, 2018) limit the outer radius of the inner disk to  $\sim 55$  au.

Also known to be a gas-rich disk on large scales, HD 141569A has a total estimated mass in the 13–200  $M_\oplus$  ( $0.39$ – $6.0 \times 10^{-4} M_\odot$ ) range (Zuckerman et al. 1995; Jonkheid et al. 2006; Thi et al. 2014; Flaherty et al. 2016). The CO rovibrational emission lines trace the existence of the gas between 17 and 500 au (Brittain et al. 2003; Goto et al. 2006; Flaherty et al. 2016; White et al. 2016). However, spatially resolved ALMA  $^{12}\text{CO}$  ( $J=3-2$ ) observations reveal that the  $< 210$  au region of the disk may contain only a fraction,  $\sim 1.5 M_\oplus$  ( $4.5 \times 10^{-6} M_\odot$ ), of this gas mass (White et al. 2016), and that the inner  $< 50$  au hold only tenuous amounts of CO gas.

We present the first  $H$ -band polarimetric observations of the inner disk of HD 141569A (Section 2). We use polarimetric differential imaging (PDI) with the Gemini Planet Imager (GPI; Macintosh et al. 2014). The PDI excels in high-contrast sensitivity to polarized circumstellar emission, as it eliminates the need of further point-spread function (PSF) subtraction that can hamper the detection of extended emission. Our PDI observations resolve the inner disk into a ring with polarized intensity peaking at 44 au and extending inward to  $0''.25$  (28 au; Section 3). We model the linear polarized intensity image to derive the physical parameters of the disk (Section 4). We also compare the predicted thermal emission from our best-fit model against the spectral energy distribution (SED) assembled from previous studies (Section 5). We present our conclusions in Section 6.

## 2. Observations and Data Reduction

We observed HD 141569A on 2014 March 22 UT in polarimetry mode at the  $H$  band during GPI commissioning at the Gemini South Telescope. We acquired 50 frames of 60 s each over  $45^\circ$  of parallactic field rotation at an average airmass of 1.12. Between each observation, the half wave plate (HWP) modulator was rotated in  $22.5$  steps. The HWP introduces modulation in the signal and thereby allows for reconstruction of the Stokes vector later in the reduction steps. During these observations, the average Gemini differential image motion monitor (DIMM) seeing at Cerro Pachón was  $0''.70$ .

We reduced the data with the GPI data reduction pipeline (DRP; Maire et al. 2014; Perrin et al. 2014) following the procedure described in Millar-Blanchaer et al. (2015) and Perrin et al. (2015). This starts with dark subtraction, correction for instrument flexure, microphonics noise, and bad pixels. Each frame is then assembled into a polarization data cube, where the third dimension comprises two image slices, each containing one of the two orthogonal polarization states yielded by the Wollaston prism analyzer. Each data cube is divided by a Gemini facility calibration unit flat field for throughput correction across the field. We correct for instrumental polarization as outlined in Millar-Blanchaer et al. (2015).

The position of the central star is determined using GPI’s four fiducial satellite spots (Wang et al. 2014). In broadband images, the satellite spots are smeared radially outward from the central star and form bright elongated streaks that can be

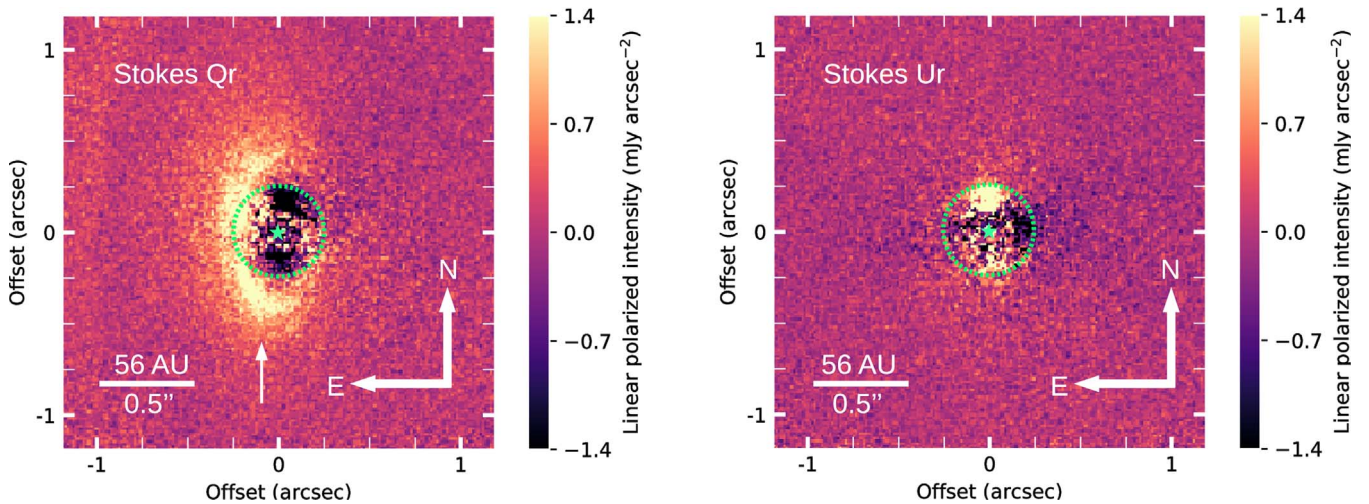


**Figure 1.** Observations of the HD 141569A dusty disk in  $H$ -band linear polarization with GPI in a total of 50 minutes of integration. Left: linear polarization intensity  $Q_r$  image. An arrow points to the location of the surface brightness enhancement—an arc feature (see Figure 8)—to the south. Right: Stokes  $U_r$  image shown on the same color scale. A star symbol marks the position of the star, and a circular aperture of radius  $0''.25$  centered on the star indicates the region affected by uncorrected instrumental polarization. Beyond this region, the  $U_r$  image scatters uniformly around zero flux, which indicates that the dust seen in the Stokes  $Q_r$  is optically thin. The previously known middle ring is visible at low surface brightness at  $1''$  to the east in the Stokes  $Q_r$  image.

used to estimate the location of the obscured star (Pueyo et al. 2015). Following Wang et al. (2014), we use a technique that implements a Radon transform of the flux distribution in each polarized image to compute the line integral over all lines passing through an initial guess for the position of the star. We sum the squares of all line integrals and repeat the procedure for the next guess for the stellar position within a small search box. The point within the search box that contains the most light pointing toward it corresponds to the stellar position. This way, we attain the position of the obscured central star to  $\sim 1$  mas precision (Wang et al. 2014). We then perform a double differencing between the two polarization states to correct for non-common path errors (Perrin et al. 2015).

We use the series of differenced data cubes obtained at different HWP angles to construct a single Stokes  $[I, Q, U, V]$  data cube, the 2D slices of which hold the total intensity and linear and circular polarization information for the entire observation sequence. The details of this procedure are presented in Appendix B.2 of Perrin et al. (2015). Because GPI’s HWP is not exactly one half wave at all wavelengths, GPI is only weakly sensitive to circular polarization, Stokes  $V$ . Thus, we disregard the Stokes  $V$  cube slice. Afterward, following Schmid et al. (2006), the Stokes cube was transformed into the radial Stokes convention  $[I, Q_r, U_r, V]$ . In this formalism, positive values of Stokes  $Q_r$  represent linear polarization perpendicular to the radial direction from the star, while negative values represent polarization parallel to the radial direction. For Rayleigh-like scatterers in an optically thin debris disk, no flux is expected in the Stokes  $U_r$  image as only the perpendicular macroscopic polarization state (azimuthal polarization) prevails (Millar-Blanchaer et al. 2015). Thus, light from single scattering events by dust grains will lead to positive values in Stokes  $Q_r$ . However, we note that multiple scattering in optically thick disks could have a Stokes  $U_r$  signal of a few percent of the Stokes  $Q_r$  signal (Canovas et al. 2015), which is below the sensitivity of our observations.

Our final reduction step is to flux-calibrate the data. Following the procedure outlined in Hung et al. (2016) and adopting  $1.85 \pm 0.07$  Jy as the  $H$ -band flux of HD 141569A from the Two Micron All Sky Survey (Cutri et al. 2003), we

obtain a conversion factor of  $(1.05 \pm 0.06) \times 10^{-8}$  Jy  $\text{ADU}^{-1}$   $\text{coadd}^{-1}$ . The final  $Q_r$  and  $U_r$  images are shown in Figure 1, and a signal-to-noise ratio (S/N) map of the  $Q_r$  image is shown in Figure 2.

In addition to the Stokes  $Q_r$  image, we also reduced the total intensity image (Stokes  $I$  slice) for the entire sequence with `pyKLIP` (Wang et al. 2015), which implements the Karhunen–Loève Image Projection (KLIP) algorithm (Soummer et al. 2012) for optimal PSF subtraction. That reduced image is shown in Figure 3.

Immediately after the polarimetry sequence was completed, we also acquired integral field spectroscopic (IFS; nonpolarimetric) observations of HD 141569A with GPI in the  $H$  band. The IFS data contain an independent measurement of the total intensity flux from the disk. The sequence comprised 32 frames of 60 s each. The sequence started at an airmass of 1.13, with an average Gemini DIMM seeing of  $1''.01$  and  $27^\circ$  of cumulative field rotation. We reduced the data and assembled the spectral data cubes with the standard recipes provided in the GPI DRP. The entire reduced data set was then processed with `pyKLIP`. However, unlike our polarimetric observations, this shorter IFS sequence did not reveal the disk and is not shown here.

### 3. Results

We present the imaging results in polarized and total intensity in Sections 3.1 and 3.2, respectively. We revisit these further in Sections 5.1 and 5.2 in the context of previous observations and a scattered-light model of the disk (Section 4).

#### 3.1. Polarized Intensity $H$ -band Image

The  $H$ -band Stokes  $Q_r$  image in Figure 1 shows the first polarized-light detection of the HD 141569A inner disk. We clearly resolve the eastern portion of the disk, likely the result of predominantly forward scattering by micron-sized dust grains. This is dictated by the combined effects of phase function and polarization dependence with scattering angle. Most known dust compositions preferentially scatter light in the forward direction for dust particles a few times larger than

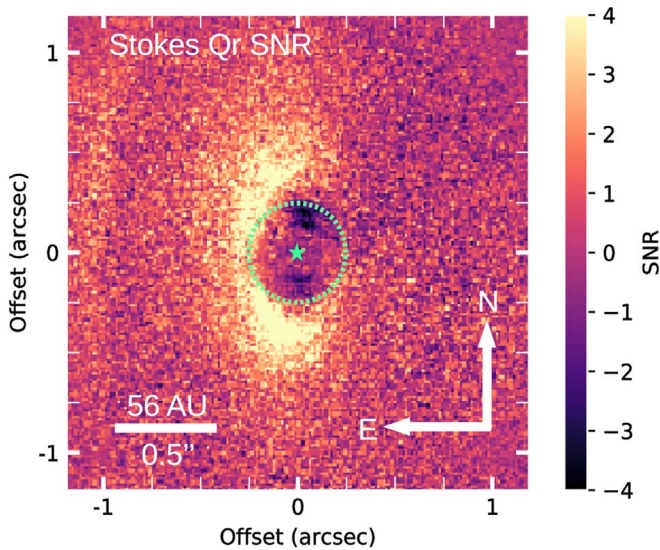


**Figure 2.** The  $H$ -band Stokes  $Q_r$  S/N map of HD 141569A. Each point on the map is constructed by dividing the  $Q_r$  image by the standard deviation of all pixels within a 3 pixel wide annulus in the  $U_r$  image at the same angular separation from the star.

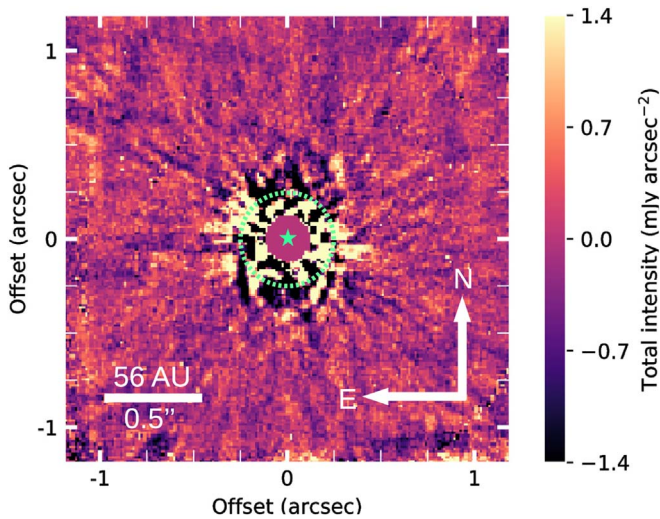


**Figure 3.** The  $H$ -band total intensity (Stokes  $I$ ) pyKLIP+ADI reduction of HD 141569A (Section 3.2). Self-subtraction degrades the residuals, and there is no significant evidence of the presence of the inner ring. The image hints at the presence of the middle 220 au ring  $1''$  to the east.

the wavelength of the scattered light (van de Hulst 1958). For such particles, optically thin Mie models also suggest that polarized intensity curves peak at scattering angles  $\leq 90^\circ$  (Perrin et al. 2015).

The emission peaks to the east at a semimajor axis of  $0''.40$  (44 au) and extends out to  $\sim 0''.9$  (100 au), where it blends into the background. At  $1''$  to the east, the Stokes  $Q_r$  surface brightness increases again, revealing the previously detected middle dusty ring at 220 au. The clearing between the inner disk and the middle ring indicates a region deficient in scattering material, assuming that the disk is optically thin.

The western part of the Stokes  $Q_r$  image shows no significant emission. We set a  $1\sigma$  lower limit of 4.0 on the ratio of forward to backward scattering in polarized intensity. If the polarization phase function is symmetric around  $90^\circ$ , then this also sets a lower limit on the forward to backward scattering intensity.

However, we do not anticipate this to generally be true, as evidenced by the unusual case of the HR 4796A debris disk (Perrin et al. 2015; Milli et al. 2017) and by theoretical projections for polarization phase functions in Canovas et al. (2015).

In Section 5.2 we further discuss a residual arc-like structure to the south, which is also detectable as a brightness enhancement in the Stokes  $Q_r$  image (Figure 1, left panel). Uncorrected instrumental polarization affects the signal within  $0''.25$  of the star. We have delimited this region with a dashed circle in Figures 1–3 and excluded it from our analysis.

No coherent structures are observed in the Stokes  $U_r$  image to indicate significant optical depth. Hence, the Stokes  $U_r$  image can be used as a noise map for our measurements, and it reassures the astrophysical nature of the Stokes  $Q_r$  emission, specifically, the polarized morphology exterior to  $0''.25$  and the middle ring near the edge to the east. Figure 2 shows an S/N map created by dividing the  $Q_r$  image at every position by local noise estimated as the standard deviation of pixels within a 3 pixel wide annulus in the Stokes  $U_r$  image at the same angular separation from the star.

### 3.2. Total Intensity H-band Image

We attempted to detect the total intensity emission from the inner ring in two different ways: from the combined polarization states in our PDI observations and from the unpolarized IFS observations. Figure 3 shows the result of the PSF subtraction of the Stokes  $I$  image after applying pyKLIP (Wang et al. 2015) and angular differential imaging (ADI; Marois et al. 2006). Our shorter IFS sequence with GPI did not reveal either the inner disk detected in Stokes  $Q_r$  or the previously known middle ring.

Our inability to detect the inner ring in total intensity is not entirely surprising. In extracting the Stokes  $I$  signal from high-contrast observations, we lose the differential imaging advantage of PDI. Moreover, the PSF subtraction process in total intensity also removes the smooth structure of the disk. Hence, we expect greater sensitivity to scattered light in our polarized-light Stokes  $Q_r$  image. In view of the low-S/N detection in total intensity, we use only the polarimetric detection in Stokes  $Q_r$  in the remainder of this study.

## 4. Disk Modeling

We model the resolved polarized Stokes  $Q_r$  image of the inner disk with a radiative transfer model to determine the disk geometry (Section 4.1) and dust properties (Section 4.2). The same modeling tool can predict the SED for the disk models, but since the SED is dominated by emission from dust outside the GPI field of view, we only compute a model SED as a test to check against gross inconsistency (Section 4.3).

### 4.1. Parameterization of the Dust Model

We use the Monte Carlo continuum radiative transfer and ray-tracing code MCFOST (Pinte et al. 2006, 2009) to compute synthetic observations of the SED and the Stokes  $Q_r$  images of the disk around HD 141569A. The MCFOST code computes the scattering, absorption, and reemission events by dust grains by propagating photon packets throughout a cylindrical spatial grid in accordance with Mie theory.

Dust grains are assumed to be in radiative equilibrium embedded in the radiation field from the host star. The sampling

of our synthetic images is defined to cover the entire field of view of observations using GPI's pixel scale of  $14.166 \pm 0.007$  mas lenslet<sup>-1</sup> (De Rosa et al. 2015). The star is located at the center of the computational grid, and the disk is centered on the star. To obtain the stellar luminosity, we fit the optical-to-near-IR SED of HD 141569A (Høg et al. 2000; Cutri et al. 2003; Mendigutía et al. 2012), keeping the stellar radius and foreground extinction as variables. We assumed a fixed distance of 111 pc with an effective temperature of 10,000 K for the star (Merín et al. 2004) and used NextGen photospheric models from Hauschildt et al. (1999). We obtain  $L = 25.48 L_{\odot}$  for the stellar luminosity. It agrees within the uncertainties with the previous estimate of  $25.77_{-1.63}^{+2.2} L_{\odot}$  by Merín et al. (2004).

The disk geometry in cylindrical coordinates is described by the radial extent of the disk, with inner and outer radii  $R_{\text{in}}$  and  $R_{\text{out}}$ , inclination  $i$ , PA, and dust density distribution  $\rho(r, z) = \Sigma(r)Z(r, z)$ . Following Augereau et al. (1999b), the dust distribution in the vertical direction is parameterized within the MCFOST framework as an exponential with a shape parameter  $\gamma$ ,

$$Z(r, z) = \exp\left(-\frac{|z|}{H(r)}\right)^{\gamma}, \quad (1)$$

where the scale height is defined as  $H(r) = H_0\left(\frac{r}{R_0}\right)^{\beta}$  at a fixed reference radius  $R_0 = 45$  au, and  $\beta$  is a disk flaring parameter. Radially, the dust distribution follows a smooth combination of two power laws,

$$\Sigma(r) \propto \left\{ \left(\frac{r}{R_c}\right)^{-2\alpha_{\text{in}}} + \left(\frac{r}{R_c}\right)^{-2\alpha_{\text{out}}} \right\}^{-1/2}, \quad (2)$$

where  $\alpha_{\text{in}} > 0$ ,  $\alpha_{\text{out}} < 0$ , and  $R_c$  is the radial distance of the peak density of the grain distribution. The surface density of dust grains is represented as

$$\sigma(r) = \int_{-\infty}^{+\infty} \rho(r, z) dz = \sigma_0 \times \Sigma(r) \left(\frac{r}{R_0}\right)^{\beta}, \quad (3)$$

where  $\sigma_0 = 2H_0\rho(R_0, 0)$  for  $\gamma = 1$ . The maximum of the surface density is not at  $R_c$  but rather at

$$r_{\text{max}(\sigma)} = \left(\frac{\Gamma_{\text{in}}}{-\Gamma_{\text{out}}}\right)^{(2\Gamma_{\text{in}} - 2\Gamma_{\text{out}})^{-1}} R_c, \quad (4)$$

where  $\Gamma_1 = \alpha_{\text{in}} + \beta$  and  $\Gamma_2 = \alpha_{\text{out}} + \beta$ , which in our case is nearly identical to  $R_c$ .

We assume a disk with a constant opening angle, thus no flaring ( $\beta = 1$ ), and adopt  $\gamma = 1$ . Without better initial constraints on these parameters, our assumption is reasonable for an optically thin debris disk.

The surface brightness and thermal flux of the disk are controlled by the total mass in grains  $M_d$  in the disk. To characterize the dust content in the disk, we adopt a power-law grain size distribution  $dN(a) \propto a^{-n} da$  with  $n = 3.5$ , as is commonly assumed for debris disks in a steady-state collisional cascade (Dohnanyi 1969). The size distribution has limits  $a_{\text{min}}$  and  $a_{\text{max}}$  and grain porosity  $p$ . We fix  $a_{\text{max}} = 1$  mm and leave  $a_{\text{min}}$  as a free parameter in the model. Within the MCFOST framework, the refractive index of porous grains is approximated from a mixture of solid grains with void particles following the Bruggeman mixing rule. Modeling is limited to a

stellocentric disk populated by a single dust grain composition of amorphous magnesium-rich olivine with a dust grain density  $\rho_{\text{dust}} = 3.5 \text{ g cm}^{-3}$ . We adopted this dust grain composition to match the composition used by Thi et al. (2014) and Mawet et al. (2017).

Our disk model parameterization thus comprises  $R_{\text{in}}$ ,  $R_{\text{out}}$ ,  $i$ , PA,  $H_0$ ,  $M_d$ ,  $\alpha_{\text{in}}$ ,  $\alpha_{\text{out}}$ ,  $R_c$ ,  $a_{\text{min}}$ , and  $p$ . To reduce the burden of an 11 dimensional parameter exploration, we fixed  $R_{\text{in}}$  and  $R_{\text{out}}$  at 20 and 110 au, respectively. These disk boundaries are motivated by our inability to detect the inner disk within  $\sim 0''.25$  and beyond  $1''$  from the star (Figure 2). We also set  $\alpha_{\text{in}} = 14$  as motivated by preliminary modeling that pointed to high  $\alpha_{\text{in}}$  values. Such a steep profile implies a sharp drop in density inside of  $r_{\text{max}}$ . The probability density distribution for  $\alpha_{\text{in}}$  in those models plateaued at  $\alpha_{\text{in}} \geq 14$ .

By exploring each of the variable parameters at 5–11 discrete values, we construct a model grid with over  $3 \times 10^7$  grid points for the remaining eight free parameters. Table 1 details the full set of parameters involved in the modeling, including additional fixed parameters for the star and disk.

#### 4.2. Polarized Scattered-light Modeling and Best-fit Estimates

In preparation for the fitting procedure, we first binned the images in  $3 \times 3$  pixels to reduce the effects of correlated errors. The GPI resolution element is about 3 pixels in the  $H$  band; therefore, the binning should not lead to a loss of spatial information. Following Millar-Blanchaer et al. (2015), we used the  $3 \times 3$  binned Stokes  $U_r$  to derive the uncertainties used to fit the binned Stokes  $Q_r$  image. For each position in the binned Stokes  $Q_r$  image, the uncertainty is calculated as the standard deviation of a 3 pixel wide annulus on the binned  $U_r$  image. These steps return the uncertainty map  $\sigma$  to use in the  $\chi^2$  minimization procedure:

$$\chi^2 = \sum_i^{\text{Npix}} \left( \frac{\text{Obs}_i - \text{Mod}_i}{\sigma_i} \right)^2. \quad (5)$$

The fitting occurs within a  $0''.85 \times 0''.61$  (radius) elliptical region centered on the star and excludes the central  $0''.25$  radius circular region to avoid PSF subtraction residuals (Figure 4, left). The fitting region in the binned image has 767 resolution elements. We opt for an elliptical fitting region rather than a circular one because Poisson noise from the disk rather than the stellar halo is the main limiting factor for our sensitivity.

The outcome of our modeling strategy is presented in Figure 4, which shows the Stokes  $Q_r$  image (left), the best-fit model (middle), and the residuals (right), all displayed on the same color and intensity scale as the Stokes  $U_r$  image in Figure 1. Our best-fit model returns a reduced  $\chi_r^2 = 0.93$  and so provides a good match to the Stokes  $Q_r$  image. Our best-fit model Stokes  $U_r$  image contains very little flux, on the order of 0.1% of the model Stokes  $Q_r$ . This indicates that the disk is optically thin with an inferred midplane optical depth of  $\tau_{1.65 \mu\text{m}} = 10^{-2}$  from MCFOST.

As a consistency check on our best-fit solution, we plot the radial profiles of the polarized emission along the semimajor axis of the disk and compare them to the prediction from the model (Figure 5). We see that the model follows the radial profile well and stays within the  $1\sigma$  uncertainty band at most separations, except inward of 31 au to the north, where it overestimates the observed emission. There is also residual emission to the south

**Table 1**  
Parameters Probed in Our Exploration Grid of Models with MCFOST and Best-fit Values for the Stokes  $Q_r$  Image

Fixed Stellar Parameters					
Distance		$d(\text{pc})$		111	
Stellar radius		$R_*(R_\odot)$		1.66	
Effective temperature		$T_{\text{eff}}(\text{K})$		10,000	
Extinction		$E_{B-V}(\text{mag})$		0.144	
		$R_V(\text{mag})$		3.1	
Disk Model Fixed Parameters					
Inner radius		$R_{\text{in}}(\text{au})$		20	
Outer radius		$R_{\text{out}}(\text{au})$		110	
Inner exponent		$\alpha_{\text{in}}$		14	
Reference radius		$R_0(\text{au})$		45	
Solid material dust density		$\rho_{\text{dust}}(\text{g cm}^{-3})$		3.5	
Flaring exponent		$\beta$		1	
Vertical exponent		$\gamma$		1	
Disk Model Free Parameters		Sampling	Range	Number of Values	Best-fit Value
Inclination	$i(^{\circ})$	Lin. in cosine	[40, 80]	10	$60^{\circ} \pm 10^{\circ}$
Position angle	PA ( $^{\circ}$ )	Lin.	[-25, 15]	9	$5^{\circ} \pm 10^{\circ}$
Reference scale height	$H_0(\text{au})$	Lin.	[2.2, 36]	9	$14_{-5}^{+9}$
Dust mass	$M_d(M_\odot)$	Lin.	$[0.2, 2.0] \times 10^{-6}$	10	$1.0 \pm 0.4 \times 10^{-6}$
Outer exponent	$\alpha_{\text{out}}$	Lin.	[-3.5, 0.0]	8	$-1.0_{-1.0}^{+0.5}$
$R_c$	$R_c(\text{au})$	Lin.	[24, 64]	11	$44_{-12}^{+8}$
Minimum grain size	$a_{\text{min}}(\mu\text{m})$	Log.	[0.5, 16]	6	$4_{-2}^{+4}$
Porosity	$p(\%)$	Lin.	[0, 20, 40, 60, 80]	5	0
Minimum reduced $\chi^2$					0.93

around PA = 150° that has no counterpart to the north (Figure 4, right) and that we discuss in Sections 5.1 and 5.2.

The overall consistency of the model and image radial profiles give us confidence that we have an adequate understanding of the dust disk parameters. Assuming that our observational errors are approximately Gaussian, and adopting a flat prior for each parameter, the Bayesian probability of our model given the data is

$$P \propto \exp\left(-\frac{\chi^2}{2}\right). \quad (6)$$

To estimate the probability density distribution for any parameter, we marginalize  $P$  over the remaining parameters as shown in Figure 6.

We obtain good constraints for  $\alpha_{\text{out}}$ ,  $M$ , and  $a_{\text{min}}$ , whose probability density distributions are approximately Gaussian. Unfortunately, our modeling returns poor constraints on the viewing geometry of the disk and some of the parameters that describe the spatial distribution of the dust. The posterior distributions for  $i$  and PA in Figure 6 are broader than we anticipated. Hence, we cannot establish a proper uncertainty. This suggests that polarized intensity alone is not adequate for determining the geometry, since only the eastern half of the disk is detected. In addition, for  $H_0$  and  $R_c$ , our modeling returns nonsymmetric skewed distributions. We use the 68% confidence intervals as estimates for the uncertainties on the best-fit parameter values for  $i$ , PA,  $H_0$ ,  $\alpha_{\text{out}}$ ,  $R_c$ , and  $M_d$ . For  $a_{\text{min}}$  and  $p$ , we use the 90% confidence interval instead, as motivated by our coarser sampling in these parameters.

Our best-fit disk model has  $i \sim 60^{\circ}$ , PA  $\sim 5^{\circ}$ , scale radius  $R_c = 44_{-12}^{+8}$  au, a rather large reference scale height  $H_0 = 14_{-5}^{+9}$  au

(which, at a reference radius of  $R_0 = 45$  au, gives an opening angle of 17°), and a shallow outer exponent  $\alpha_{\text{out}} = -1.0_{-1.0}^{+0.5}$ . The total dust mass of  $1.0 \pm 0.4 \times 10^{-6} M_\odot$  is within the range  $(0.03\text{--}1) \times 10^{-5} M_\odot$  estimated from SED modeling (Zuckerman et al. 1995; Sylvester et al. 1996; Merin et al. 2004; Thi et al. 2014). The best-fit minimum grain size is  $a_{\text{min}} = 4_{-2}^{+4} \mu\text{m}$  (90% confidence interval). The minimum grain size agrees with the blowout grain radius (Burns et al. 1979) in a gas-poor disk, with  $r_{\text{blowout}} = 4.2 \mu\text{m}$  for spherical silicate grains of density  $\rho = 3.5 \text{ g cm}^{-3}$ , assuming a radiation pressure efficiency factor of  $Q_p = 1$ . We discuss the blowout radius with respect to the gas content of the inner disk further in Section 5.4. The best-fit model favors a population of solid dust grains with porosity  $p = 0\%$ , although it is consistent with porosity up to  $p = 40\%$  within the 90% confidence limit.

As seen in Figure 6, the total dust mass  $M_d$  is strongly degenerate with several disk parameters, notably the minimum grain size  $a_{\text{min}}$ , the outer exponent  $\alpha_{\text{out}}$ , and, surprisingly, the disk scale height  $H_0$ . There is no evident mechanism by which the scale height would be degenerate with the disk mass for an optically thin disk. A third parameter could set this correlation, but the relationship remains unclear. All of these degeneracies preclude us from placing fully independent constraints on  $M_d$ ,  $a_{\text{min}}$ ,  $H_0$ , or  $\alpha_{\text{out}}$ . In Section 5.4 we discuss an independent and more stringent constraint on the minimum grain size  $a_{\text{min}}$  arising from the lack of measurable signal in the Stokes  $U_r$  image.

### 4.3. Comparison of the Scattered-light Model to the SED

We compare the predicted thermal emission from our best-fit model to the Stokes  $Q_r$  image against the SED of HD 141569A

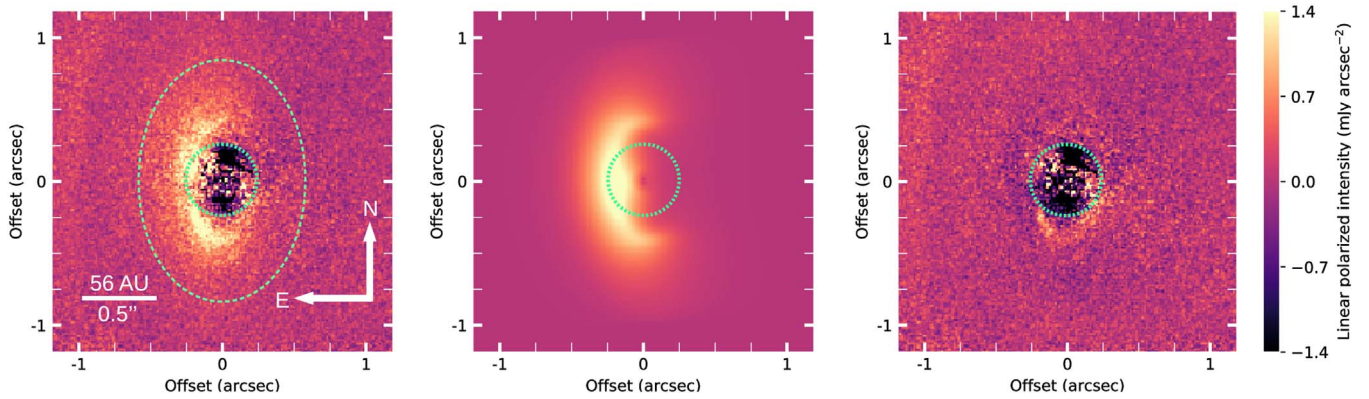


**Figure 4.** Modeling of the inner HD 141569A dust ring with MCFOST. The central  $0''.25$  circular region is the same as in Figures 1–3 and is ignored in the modeling. Left: observed Stokes  $Q_r$  image with the fitting region delimited between the circular and elliptical dashed lines. Middle: Stokes  $Q_r$  image from the best-fit model. Right: residuals of the Stokes  $Q_r$  image minus the best-fit model. A residual arc-like polarized emission is seen to the south. We have used the same intensity scale and color stretch as for the Stokes  $U_r$  image in Figure 1.

in Figure 7. Fitting the SED is not a part of our search for the model that best matches the scattered-light emission. It is merely a consistency check on our scattered-light modeling, assuming that the same dust population is responsible for both disk tracers.

We use the compendium of photometric data from Thi et al. (2014) with updated photometry in the optical (Høg et al. 2000; Mendigutía et al. 2012). We expand this data set by including recent submillimeter and millimeter photometry with ALMA (White et al. 2018) and the Submillimeter Array (SMA; Flaherty et al. 2016). We note that the photometric measurements in Thi et al. (2014), Flaherty et al. (2016), and White et al. (2018) come from instruments with different resolutions and beam sizes. These range from FWHM  $\approx 1''$  seeing-limited optical/near-IR measurements, to a beam of  $5''.1 \times 4''.2$  for the 2.8 mm SMA photometry, up to  $2' \times 5'$  for  $60 \mu\text{m}$  photometry from the *Infrared Astronomical Satellite* (IRAS).

We also include a polycyclic aromatic hydrocarbon (PAH) component, motivated by resolved (FWHM =  $0''.26$ ) observations with the VLT Imager and Spectrometer for the mid-IR (VISIR; Lagage et al. 2004) in the PAH1 filter ( $\lambda_c = 8.6 \mu\text{m}$ ,  $\Delta\lambda = 0.42$ ). These reveal a disk out to  $1''$  along the semimajor axis (Thi et al. 2014). The PAHs in the circumstellar environment of HD 141569A are responsible for the emission features in the mid-IR at 7.7, 8.7, 11.3, and  $12.7 \mu\text{m}$  (Sylvester et al. 1996). We include the PAH component (magenta dotted line) with the sole goal of approximating the emission features in the mid-IR modeled in previous studies (Li & Lunine 2003; Thi et al. 2014). The PAHs were added with the adopted single molecule size of  $6.84 \text{ \AA}$  and fixed mass of  $1.6 \times 10^{-10} M_\odot$  from Thi et al. (2014).

The thermal emission from our scattered-light model of the 44 au disk reproduces the observed  $\geq 50 \mu\text{m}$  fluxes adequately. The emission peaks at a wavelength of  $45 \mu\text{m}$  (and so has a characteristic dust temperature of 67 K) and a flux of  $1.6 \times 10^{-13} \text{ W m}^{-2}$ . This is within factors of 1.0–1.8 of the observed 60– $100 \mu\text{m}$  far-IR fluxes measured with *IRAS*, *Spitzer*, and *Herschel* (Thi et al. 2014, and references therein). The range is entirely due to the scatter in the flux measurements from different instruments.

At  $>140 \mu\text{m}$  wavelengths, the predicted thermal emission from the 44 au disk matches the SED unexpectedly well, considering

that we did not include any SED information in our modeling. The published far-IR and millimeter flux measurements are obtained from much wider beams that incorporate the outer two debris rings, so we expect that the fluxes should be higher than the predicted brightness of the 44 au ring. While an SED analysis of HD 141569A is relegated to a future study, there are two independent lines of evidence that suggest that the 44 au ring dominates the  $>100 \mu\text{m}$  thermal emission. First, the emission resolved in the ALMA  $870 \mu\text{m}$  continuum and CO maps in White et al. (2016) is consistent with an origin in an  $\sim 50$  au ring, likely the same dust ring as resolved by GPI. ALMA shows no evidence of significant millimeter emission associated with the middle (220 au) dust ring. Second, with the middle dust ring being about five times wider than the inner 44 au ring, its characteristic dust temperature will be  $\sim\sqrt{5}$  cooler, so  $\sim 30$  K. A strong 30 K dust component will produce a notable bump in the SED around  $100 \mu\text{m}$ . However, the observed  $\geq 60 \mu\text{m}$  fluxes closely follow a Rayleigh–Jeans distribution. Hence, we believe that the 44 au dust disk resolved by GPI accounts for most of the long-wavelength flux from the HD 141569A circumstellar disk.

Finally, we note that even while it reproduces the observed  $\geq 60 \mu\text{m}$  fluxes adequately, the combined SED of our scattered light and PAH emission model is underluminous between 8 and  $30 \mu\text{m}$ . A fourth component, interior to the one seen by GPI, is likely present around the star. To correct for this flux deficit in the mid-IR, we model an innermost 5–15 au dust disk (light blue dashed line in Figure 7) in MCFOST. We discuss this innermost disk further in Section 5.5.

#### 4.4. The Effect of Mie Scattering Assumptions on Disk Modeling Results

The synthetic models in our modeling procedure rely on Mie scattering theory to compute the scattering, opacity, and absorption cross sections of dust grains in the circumstellar environment of HD 141569A. Although Mie theory has been extensively used in numerous debris disk studies, it has limitations.

In Mie scattering, individual dust grains are idealized as uniform solid spheres, an assumption likely not applicable to dust grains growing through agglomeration in debris disks. Hence, Mie theory could struggle to accurately predict the light

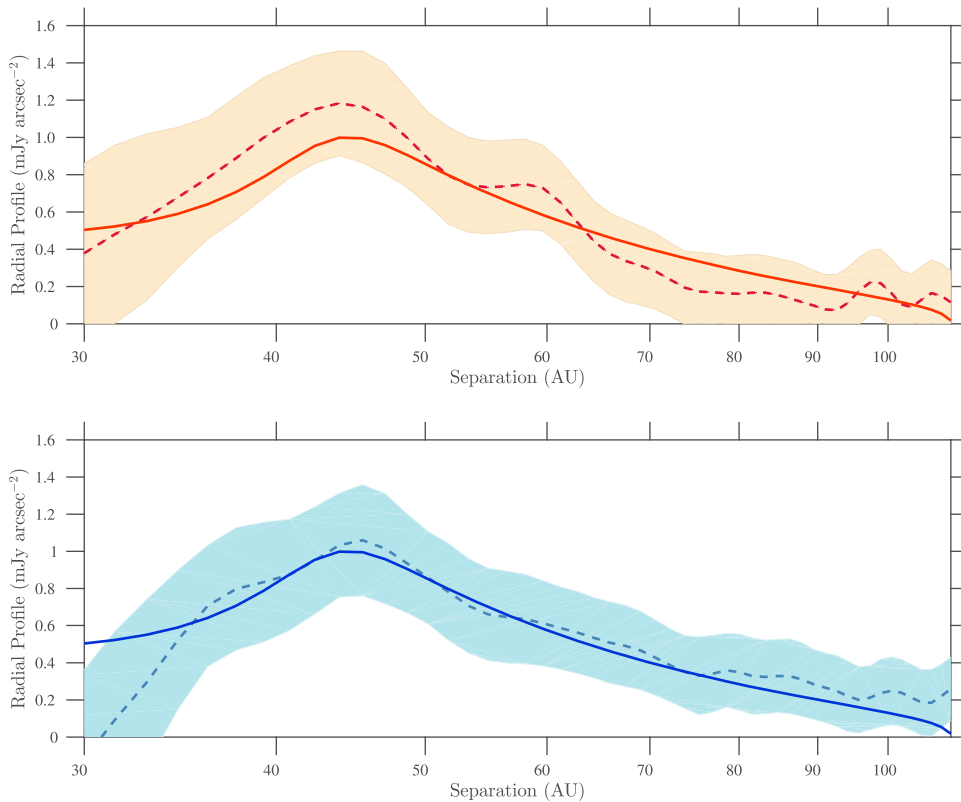


**Figure 5.** Radial profiles along the semimajor axis ( $PA = 5^\circ$ ) of the Stokes  $Q_r$  image (dashed line) and the best-fit models with MCFOST (solid line) inward to 30 au ( $0''.27$ ), north (top) and south (bottom). Shaded areas indicate the dispersion calculated using the uncertainty map derived from the Stokes  $U_r$  image (Figure 1, right panel). The best-fit model falls within the uncertainties and in general agrees with the observed profiles.

scattering and thermal processes in debris disks. More elaborate models with irregularly shaped dust grain aggregates indicate that Mie theory does not reproduce well the scattering phase function at angles  $\theta > 90^\circ$  (Min et al. 2016). Accordingly, Milli et al. (2017) showed that Mie models fail to reproduce the scattering phase function for the HR 4796A dusty debris ring. Such discrepancies likely bias the determination of certain model parameters, in particular the viewing geometry, minimum grain size, dust composition, dust mass, and porosity.

While we have adopted Mie theory-based models for our analysis for the sake of comparison with previous radiative transfer modeling on the dust-scattered light from the HD 141569A debris disk (Jonkheid et al. 2006; Thi et al. 2014; Mawet et al. 2017), we note the above limitations ahead of the ensuing discussion.

## 5. Discussion

### 5.1. Morphology of the HD 141569A Inner Disk in Polarized Scattered Light: Comparison to Previous Observations

The clearest view of the inner disk around HD 141569A inward to an inner working angle (IWA) of  $0''.25$  (28 au) was revealed by PDI with GPI. The IWA achieved with GPI shows the 44 au ring morphology that supersedes any lower-S/N detections from images with larger IWAs.

The highest S/N previously obtained on the 44 au ring in scattered light is through  $L_p$ -band AO and vortex coronagraphy with Keck/NIRC2 (FWHM  $\approx 0''.08$ , effective IWA  $\approx 0''.16$ ) by Mawet et al. (2017) and also reported with Keck/NIRC2 in the  $L_p$  band by Currie et al. (2016) down to  $0''.25$ . Perrot et al. (2016) reported even higher angular resolution  $H$ -band AO

observations with VLT/SPHERE (FWHM  $\approx 0''.040$ , IWA =  $0''.093$ ), as did Konishi et al. (2016) with *HST*/STIS (FWHM =  $0''.04$ , IWA =  $0''.40$ ). Compared to our PDI with GPI, all of these previous nonpolarimetric observations have lower S/N because of the inability to employ simultaneous differential imaging through polarimetry but relying solely on ADI instead. Diffuse structures with significant axial symmetry, such as a debris disk seen at low-to-moderate inclinations, are challenging to extract with ADI/KLIP. A high-S/N detection of the disk with much lower reduction-dependent systematics has been produced by PDI with GPI.

Our GPI polarized-light image confirms the clearing within the 44 au ring first reported by Perrot et al. (2016). Thi et al. (2014), Konishi et al. (2016), and Mawet et al. (2017) reported PAH or scattered-light emission from dust at similar separations but described its radial dependence with a single-exponent power law that decreases with separation. As seen in Figure 5, we clearly resolve the peak at 44 au that is well modeled with exponential drop-offs on either side. The width of the ring in polarized light (FWHM  $\sim 30$  au) is greater than reported (FWHM  $\sim 10$  au) from the unpolarized VLT/SPHERE observation of Perrot et al. (2016), which we attribute to self-subtraction in the various KLIP reductions of the SPHERE images.

Consistent with Perrot et al. (2016) and Mawet et al. (2017), we find a north–south asymmetry in the brightness of the 44 au ring, which we now reveal as a high-S/N arc-like structure to the south. We do not see evidence of the other clumps reported in these studies and suspect that they may be related to image artifacts.

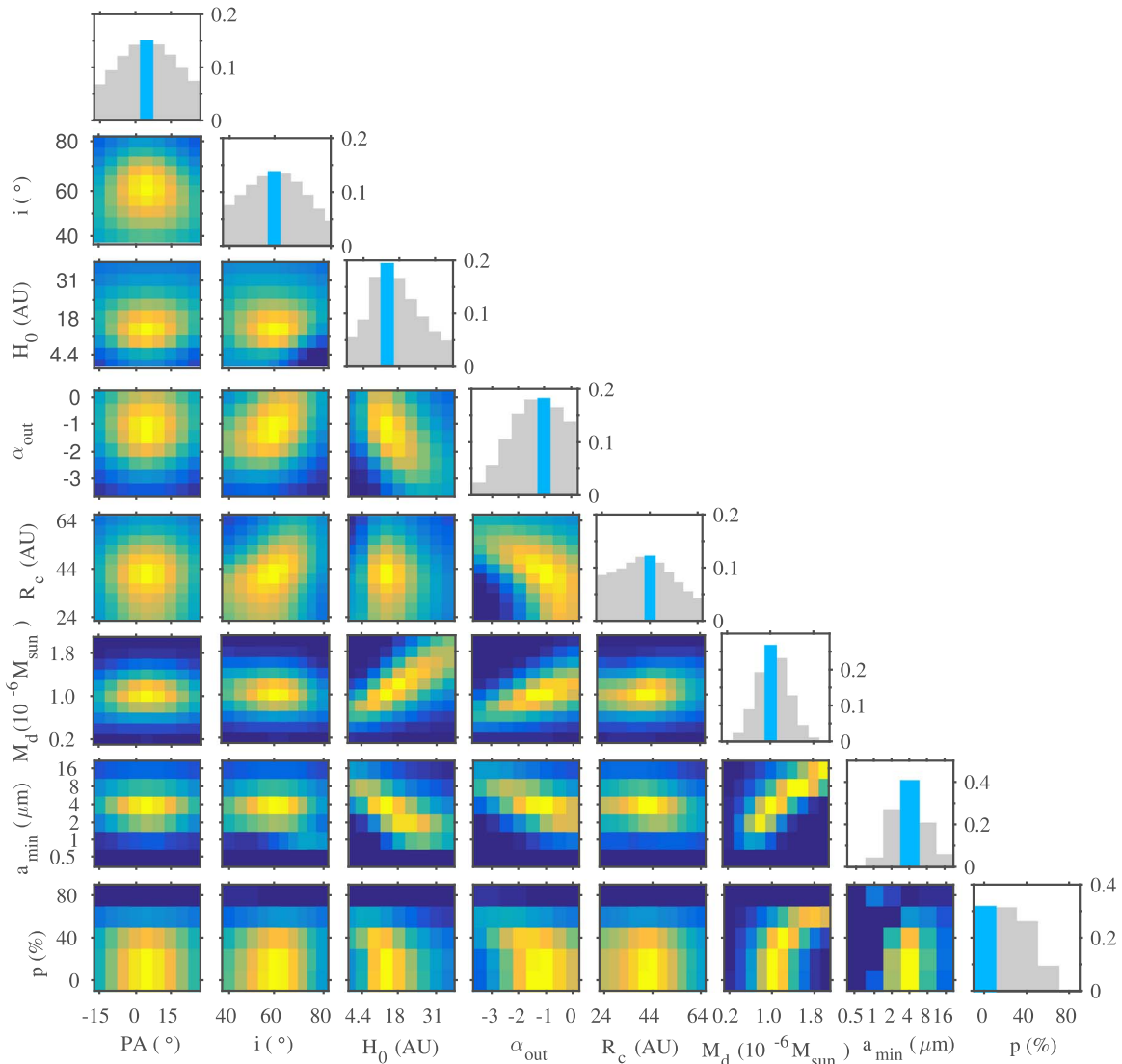


**Figure 6.** Normalized probability density distributions for each parameter in the grid of models explored to fit the Stokes  $Q_r$  image with MCFOST. Brighter yellow regions in the color maps correspond to higher probability densities. A blue bar in each of the histogram panels along the diagonal shows the best-fit value for each parameter.

The viewing geometry of our best-fit model,  $i \sim 60^\circ$  and  $PA \sim 5^\circ$ , is similar to previous findings from scattered-light total intensity observations at lower S/N. Perrot et al. (2016) reported that the inner ring has an inclination of  $i = 57.9 \pm 1.3$  and a PA of  $353.7 \pm 1.1$  from observations with VLT/SPHERE, while Mawet et al. (2017) reported  $i = 53 \pm 6^\circ$  and  $PA = 349 \pm 8^\circ$  from  $L_p$  observations with Keck/NIRC2. However, unlike all previous direct imaging (nonpolarimetric) observations, which point to a relatively well-constrained slightly west of due north orientation of the semimajor axis of the inner ring, our polarimetric observation produces a less well constrained, slightly east of due north PA. Our values for  $i$  and PA follow broad distributions in Figure 6 that suggest uncertainties of about  $10^\circ$ . Our own lower-S/N  $H$ -band total intensity image (Figure 3) suggests a slightly clockwise ( $PA \sim 350^\circ$ ) orientation of the scattered-light emission, in agreement with Perrot et al. (2016) and Mawet et al. (2017) and contrary to our polarized image. Effectively, the orientation of the inner disk from previous total intensity observations is in good alignment with the outer disk, whereas the PDI observations are less conclusive.

It is at first surprising that our polarimetric image does not produce better constraints on the geometry. The S/N of all of our own and the previously published total intensity observations is much lower. The reduced total intensity images also suffer from the typical PSF subtraction systematics for extended emission around bright stars, the result of ADI mode observations and image reduction with the KLIP algorithm. Thus, it is possible that the uncertainties in Perrot et al. (2016) have been underestimated, and our values are closer to agreement with theirs because of larger uncertainties (as in Mawet et al. 2017). Nonetheless, the discrepancy between the polarized and the total intensity geometry is still unusual, as is the inability to get better geometric constraints from our polarized intensity images.

We suspect that the failure of our modeling to produce better viewing geometry constraints may be a consequence of detecting only half of a radially extended disk in polarized intensity. The detection of this nonaxisymmetric half disk, combined with the broader arc-like feature to the south (Section 4.2; Figure 4, right), may favor models with PAs flipped around the north–south axis. In addition, as discussed in

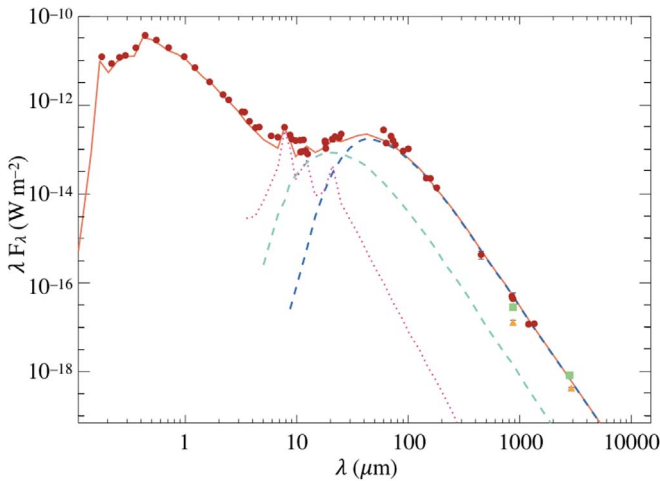


**Figure 7.** Measured data points and predicted MCFOST SEDs. Observations comprise the photometric compendium by Thi et al. (2014) and references therein (filled circles), SMA photometry by Flaherty et al. (2016; filled squares), and ALMA photometry by White et al. (2018; filled triangles). The model SEDs represent the best-fit model to the Stokes  $Q_r$  image of the HD 141569A inner disk (dark blue dashed line), a fourth innermost disk (light blue dashed line), and PAH emission (magenta dotted line). The total emission from these components and the star is shown with a solid line.

Section 4.4, it is possible that the scattering phase function derived in our Mie-based radiative transfer MCFOST model may not agree well with the behavior of debris disk dust grains. The detected side of the debris ring is seen at a  $>90^\circ$  scattering phase angle, and, as in the case of the HR 4796A debris ring (Milli et al. 2017), the polarization and intensity of the scattered light may not be well represented by Mie theory.

### 5.2. The Arc-like Structure: A Spiral Arm?

The arc-like asymmetry spans between  $120^\circ$  and  $170^\circ$  in PA. This feature is not an outcome of the data reduction process because the PDI image requires no further PSF subtraction; rather, it is a true brightness enhancement in the ring. A disk with a stellocentric offset could offer a possible explanation for the enhanced emission from the arc-like structure to the south. The portion of the disk closer to the star would appear brighter than the other side, leading to pericenter glow (Wyatt et al. 1999). Our modeling procedure did not include stellocentric offsets, so we cannot check for pericenter glow. Perrot et al. (2016) found that the inner ring has a stellocentric offset of  $15.4 \pm 3.4$  mas ( $1.7 \pm 0.4$  au) to the west but only a negligible one,  $1.2 \pm 9.4$  mas ( $0.1 \pm 1.1$  au), to the north. Therefore, a north–south stellocentric offset is not the likely cause of the brightness enhancement to the south.

For a clearer view of the morphology of the asymmetry, we mirror and subtract the northern portion of the disk from the southern half. Given the ambiguity of the disk’s orientation, we perform two different subtractions. In the first case, we mirror around the semiminor axis of the best-fit model of the polarized emission seen with GPI; i.e., the PA of the semimajor axis is  $5^\circ$  (Figure 8, middle panel). In the second case, we use the geometry inferred from the total intensity image from SPHERE, with a semimajor axis PA of  $353^\circ.7$  (Figure 8, right panel). Both subtractions show the excess emission to the south as a remnant arc at S/N levels of 4–5 per GPI pixel along the peak of the emission. The residuals in the PA =  $5^\circ$  case are closer to zero, which is why our modeling of the polarized-light

emission prefers that geometry. In this case, the arc contributes up to 40% of the surface brightness of the debris disk in the range  $120^\circ < \text{PA} < 170^\circ$  and has a net integrated surface brightness of  $\approx 5$  mJy within a 10 au wide region centered on the peak emission at 44 au. In the semimajor axis PA =  $353^\circ.7$  case, the residuals are more uniform, and also more positive. The arc contributes 50% of the disk surface brightness at PA =  $130^\circ$  and wraps counterclockwise to at least PA =  $190^\circ$ , where it is still at  $\sim 40\%$  of the disk’s total brightness before the signal diffuses into the residual noise. The net integrated surface brightness of the arc in the same  $120^\circ < \text{PA} < 170^\circ$  region is  $\sim 15$  and 25 mJy if extended up to PA =  $190^\circ$ .

Without a higher-S/N total intensity image of the disk, we cannot decide in favor of one disk PA versus the other. However, both point to the existence of an arc on the inner ring of the HD 141569A disk that contributes between 40% and 50% of the total disk flux to the southeast. Such arc-like structures are known on the outer two rings of HD 141569A (Mouillet et al. 2001; Clampin et al. 2003; Perrot et al. 2016; Mawet et al. 2017). We believe this to be the first convincing detection of such an arc on the inner ring. The location and extent of the feature match the observed brightness enhancement in the southeast section of the inner ring in Perrot et al. (2016) and the enhancement in the CO zeroth-moment map in White et al. (2016). Our best-fit model indicates an average temperature of  $\sim 90$  K at the location of the arc, well above the sublimation point of CO. The CO production mechanism may thus be linked to the dust overdensity, pointing to ongoing destruction of CO ice-rich planetesimals. The destruction cascade itself may be triggered by an unseen body that is also responsible for producing the arc as a spiral arm.

Spiral arm structures have been discovered in near-IR scattered-light imaging observations of a few circumstellar disks (e.g., AB Aur, Hashimoto et al. 2011; HD 142527, Avenhaus et al. 2014; SAO 206462, Muto et al. 2012; MWC 758, Grady et al. 2013; HD 100453, Wagner et al. 2015). Two mechanisms are capable of driving such arms in gas-rich protoplanetary (and transition) disks: gravitational instability (e.g., Dong et al. 2015a) and interaction between the disk and a planetary or stellar companion (e.g., Dong et al. 2015b, 2016b). In optically thin debris disks with much lower gas-to-dust ratios, photoelectric instability (Klahr & Lin 2005; Besla & Wu 2007) may also lead to clumping of dust into structures. Spiral density waves are one of the hypotheses invoked for explaining the radially moving dust enhancements in the edge-on AU Mic debris disk (Boccaletti et al. 2015). However, typically, multiple rings and arcs (i.e., broken rings), instead of one or two spiral arms, are seen in simulations (Lyra & Kuchner 2013; Richert et al. 2018). While the HD 141569A disk is almost certainly too low in mass to be gravitationally unstable, the possibility that the detected spiral arm–like feature is driven by an unseen planet is exciting. Dong et al. (2016a) showed that spiral arms driven by giant planets in disks at modest-to-high inclinations may appear very close to, or be part of, the disk ring sculpted by the planet. In particular, the  $50^\circ$  and  $60^\circ$  inclination panels in Figure 8 of Dong et al. (2016a) show intriguing similarities with the HD 141569A inner disk spiral arm in Figure 7. The weak contrast of the arm in HD 141569A indicates that if it is planet-driven, the planet is most likely Jovian or smaller (Dong & Fung 2017).

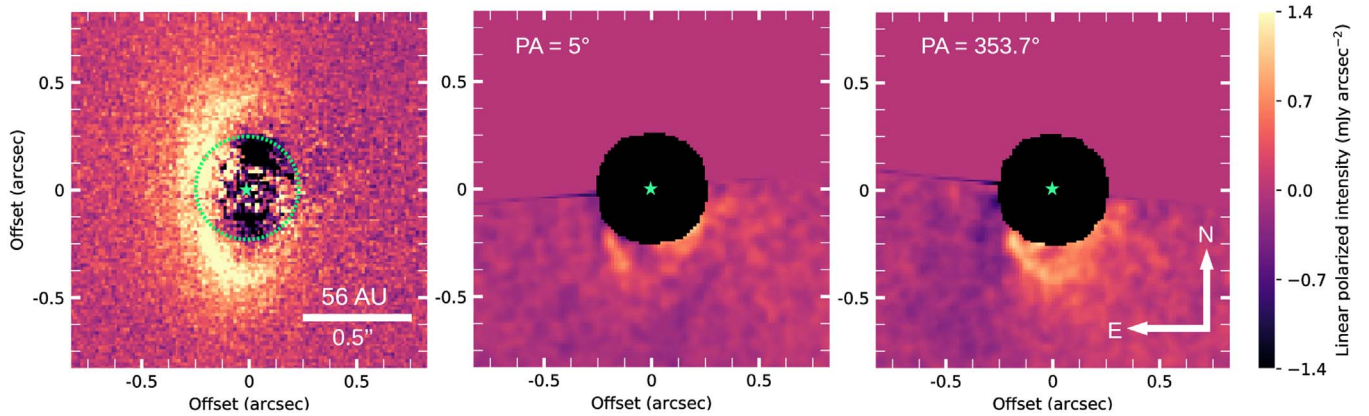


**Figure 8.** Revealing the southern arc on the 44 au dust ring around HD 141569A by mirroring the northern part of the disk and subtracting it from the southern part. Left: polarized intensity image from GPI. Middle: mirroring and subtraction, assuming the best-fit geometry of the model of the GPI polarized-light  $H$ -band emission. The arc extends over  $120^\circ$ – $170^\circ$  and contributes  $\sim 40\%$  of the total disk brightness level. Right: mirroring and subtraction, assuming the inferred geometry of the SPHERE total intensity  $H$ -band emission. The arc can be traced counterclockwise to at least  $190^\circ$  at  $40\%$ – $50\%$  of the overall disk brightness.

### 5.3. Disk Opening Angle

While it is a much less powerful constraint than it is in (optically thick) protoplanetary disks, our modeling allows us to place approximate constraints on the opening angle or scale height of the resolved inner disk. The best-fit model indicates a rather large reference scale height of  $H_0 = 14$  au at the  $R_0 = 45$  au reference radius, so an opening angle of  $17^\circ$ . This is above expectations even for a transitional disk, although values as small as  $10\%$  are within the  $84\%$  confidence limit. With such a large disk opening angle, the best-fit model incorporates significant scattering at angles smaller than the  $\sim 30^\circ$  expected from a perfectly flat disk (given an inclination of  $i \sim 60^\circ$ ). However, if our Mie theory–derived scattering phase function is wrong, this constraint is not to be trusted.

Previous determinations of the opening angle range from  $5\%$ – $10\%$  (Thi et al. 2014) to  $23\%$  (Merín et al. 2004). The latter is from SED fitting alone, and, while consistent with our finding, it is not very well constrained. The Thi et al. determination pertains to the gas disk geometry and is constrained from *Herschel* measurements of the  $[\text{C II}]/\text{CO } J=3-2$  line flux ratio, which traces the efficiency of CO photodissociation as a function of gas scale height. However, without having spatially resolved the inner disk, Thi et al. adopted a model with a gas surface density peak at  $\approx 28$  au (Figure 6 in that paper), whereas we resolve the brightness peak of the inner dust disk at 44 au (Figure 5). If the gas and dust are well mixed, as assumed by Thi et al., then a cooler gas disk would require a greater scale height to produce the same  $[\text{C II}]/\text{CO } J=3-2$  line flux ratio. It is therefore likely that under the joint constraints from the *Herschel* gas abundances and the GPI-resolved dust disk morphology, the gas disk has a  $>10\%$  opening angle, consistent with the wide dust disk opening angle found here.

### 5.4. Independent Constraint on the Minimum Grain Size from Polarimetry

Our model of the polarized scattered light (Section 4.2) produced a minimum grain size of  $a_{\min} = 4_{-2}^{+4} \mu\text{m}$ , consistent with the  $4.2 \mu\text{m}$  blowout grain radius around HD 141569A. The result for the blowout radius is meaningful as long as the inner disk remains gas-poor. Conversely, in gas-rich disks with interstellar medium–like gas-to-dust ratios of  $\sim 100$ , gas drag dominates the dynamics of small grains.

Based on a total gas mass estimate of  $200 M_{\oplus}$  ( $6 \times 10^{-4} M_{\odot}$ ), Thi et al. (2014) found an average gas-to-dust ratio of  $50$ – $100$  over the full extent of the  $\sim 500$  au disk. This would preclude a meaningful radiation pressure estimate of the blowout radius. However, White et al. (2016) found a much lower ( $\text{H}_2$ ) gas mass of  $1.5 M_{\oplus}$  within 210 au and observed that the inner  $\sim 50$  au region shows only tenuous CO emission. Hence, the inner disk that we resolved with GPI is substantially more deprived of gas. Adopting the White et al. (2016) gas mass and our best-fit dust mass of  $\sim 10^{-6} M_{\odot} = 0.3 M_{\oplus}$  for the 44 au ring (Table 1) yields a gas-to-dust ratio of  $\sim 5$ . The actual gas-to-dust ratio in the 44 au ring is likely lower, since the White et al. (2016) gas mass estimate encompasses both the inner 44 au and parts of the middle 220 au ring. Therefore, we expect that the smallest grains in the inner ring are more strongly affected by radiation pressure than gas drag.

Our best-fit value of  $a_{\min} = 4_{-2}^{+4} \mu\text{m}$  for the minimum grain size is marginally consistent with previous findings from scattered-light observations (Marsh et al. 2002; Mawet et al. 2017) but differ from values inferred from SED modeling (Thi et al. 2014; Mawet et al. 2017). The resolved Keck II mid-IR observations of Marsh et al. (2002) yield a best-fit ( $\chi^2_{\nu} = 1.23$ ) minimum grain size of  $1$ – $3 \mu\text{m}$ —in agreement with our findings—although fits with either interstellar medium–sized  $0.1 \mu\text{m}$  ( $\chi^2_{\nu} = 1.40$ ) or large ( $\gtrsim 30 \mu\text{m}$ ) blackbody grains ( $\chi^2_{\nu} = 1.50$ ) are also satisfactory. Using Mie scattering assumptions and MCFOST for modeling, Mawet et al. (2017) found that a population of dust particles of pure olivine with  $a_{\min} = 10 \mu\text{m}$  provides the best fit to the resolved  $L_p$ -band scattered-light emission between 20 and 90 au. At the same time, Mawet et al. also found that a minimum grain size of  $0.5 \mu\text{m}$  best fits the SED, echoing the findings from SED model fitting by Thi et al. (2014). The combined best fit to the  $L_p$  image and SED in Mawet et al. (2017) yields an even smaller minimum grain size:  $a_{\min} = 0.1 \mu\text{m}$ .

The preference for very small ( $0.1$ – $0.5 \mu\text{m}$ ) grains in SED modeling points to the presence of a warm dust component that may not be well represented by an extrapolation of an index  $n = 3.5$  (collisionally dominated) grain size distribution below  $1 \mu\text{m}$ . The collisional cascade may not be equally efficient at all grain sizes or radial separations in the disk. Such is the case at least for large grains around HD 141569A, as multiband  $0.9$ – $9$  mm

ALMA and Very Large Array observations show that at millimeter sizes, the index is  $n = 2.95 \pm 0.1$  (White et al. 2018).

Our polarization observations are uniquely diagnostic of the presence of submicron grains because of their polarization properties. Specifically, scattered-light models with a significant population of  $a_{\min} < 0.8 \mu\text{m}$  are rejected because they produce negative polarization in Stokes  $Q_r$  that is not observed by GPI. We similarly rule out highly porous ( $p > 60\%$ ) materials. Thus, with the added power of near-IR polarimetry, we conclude that the population of  $\leq 1.0 \mu\text{m}$  grains in the 44 au dust ring is not significant enough to be detectable in polarized light. A trace population may nonetheless exist and could be responsible for the observed PAH emission. We use this result to argue for a fourth innermost and unseen component of the HD 141569A debris disk in Section 5.5.

We again caution that this analysis is rooted in Mie theory, which may not yield the correct ratio of scattered to absorbed (and emitted) flux. A non-Mie treatment could yield different constraints on the minimum grain size from the observed polarization signatures. However, an additional argument against the presence of a large reservoir of submicron grains is the lack of a  $10 \mu\text{m}$  silicate feature in the *Spitzer* IRS spectrum of HD 141569A (Sloan et al. 2005), as also argued by Thi et al. (2014). Hence, we find that a warm ring of dust grains several microns in size and lying interior to the one resolved with GPI offers the simplest explanation for the extra 8–30  $\mu\text{m}$  emission from HD 141569A.

### 5.5. An Unseen Innermost (Fourth) Ring

Our best-fit model to the light-polarizing dust offers a good match to the  $\lambda \gtrsim 50 \mu\text{m}$  SED (Figure 7). However, there is remnant excess emission between 8 and 30  $\mu\text{m}$  that is not reproduced by our dust model. The presence of warm circumstellar material well within 100 au has been inferred not only from the abovementioned SED fitting by Thi et al. (2014) and Mawet et al. (2017) but also from CO observations (Fisher et al. 2000; Merín et al. 2004; Goto et al. 2006; Thi et al. 2014; Flaherty et al. 2016; White et al. 2016). Our detection of an inner clearing within the 44 au ring and the lack of polarization signal from submicron-sized grains (Section 5.4) imposes new constraints on the spatial extent of the warm dust responsible for the excess thermal emission at shorter wavelengths.

To account for this missing flux, we employ a simple model in MCFOST assuming the same grain size distribution,  $a_{\min} = 4 \mu\text{m}$ ,  $a_{\max} = 1 \text{ mm}$ , porosity of 0%, and magnesium-rich olivines from our best-fit model. Motivated by Thi et al. (2014), the dust is characterized by a radial density distribution  $R \propto r^p$  with  $p = 1$ , no flaring ( $\beta = 1$ ), and an inner disk radius of  $R'_{\text{in}} = 5 \text{ au}$ . We keep the outer radius  $R'_{\text{out}}$  and dust mass  $M'_{\text{dust}}$  of the innermost disk as free parameters.

The best-fit thermal model for the innermost disk (light blue dashed line in Figure 7) indicates 300 K dust with a mass of  $10^{-8} M_{\odot}$  ( $3 \times 10^{-3} M_{\oplus}$ ) ranging from  $R'_{\text{in}} = 5.0 \text{ au}$  up to  $R'_{\text{out}} = 15 \text{ au}$ . This is well within the coronagraph IWA of GPI and thus presently undetectable in scattered light.

## 6. Conclusion

We have presented the first polarimetric detection of the inner 44 au disk component of the pre-main-sequence star HD 141569A. Our *H*-band PDI with GPI has revealed that there is a nonuniform ring-shaped optically thin dusty disk inward to  $0''.25$  at the highest S/N attained to date. We find that the disk

can be described radially with a combination of two power laws that peaks at 44 au and extends out to 100 au. The disk also features an arc-like overdensity along the southern part that is reminiscent of the spiral arm structures previously known at larger scales in this system. The existence of this inner spiral arm structure and its collocation with CO emission detected by ALMA indicates that this may be a site of ongoing icy grain destruction, perhaps driven by an unseen planetary perturber. The best-fit model to our polarimetry data indicates an optically thin disk with a maximum surface density of  $r_{\text{max}} \simeq R_c = 44_{-12}^{+8} \text{ au}$ , a steep inner gradient ( $\alpha_{\text{in}} = 14$ ), and a shallower outer exponent ( $\alpha_{\text{out}} = -1.0_{-1.0}^{+0.5}$ ). The polarimetric observations are best described by a dust population model with a minimum size of  $4_{-2}^{+4} \mu\text{m}$  and a mass of  $(1.0 \pm 0.4) \times 10^{-6} M_{\odot}$  for nonporous grains up to 1 mm in size. A significant population of submicron grains is independently excluded by the lack of negative signal in the *H*-band Stokes  $Q_r$  image. We use the thermal emission from our best-fit Mie model to estimate the amount of unseen dust inward of 28 au. We find that a fourth innermost dust population, potentially a 5–15 au belt, is required to fully reproduce the 8–30  $\mu\text{m}$  SED under Mie theory assumptions.

With our new high-S/N polarimetric detection of the 44 au ring, the richness of the circumstellar environment around HD 141569A can be appreciated in a new light. Considering resolved imaging data from other high-contrast facilities, the HD 141569A debris disk shapes up to be made of at least three, and potentially four, nested rings, with spiral structures on the three spatially resolved rings. As such, it is an excellent laboratory for studying dynamically perturbed disks.

We thank our referee for very insightful feedback on the dust considerations in our modeling. This research was supported in part by a Discovery Grant by the Canadian Natural Sciences and Engineering Council (NSERC) to S.M. and NSF grant AST-1413718 (GD). P.K. and J.R.G. are thankful for support from NSF AST-1518332 and NASA NNX15AC89G and NNX15AD95G/NEXSS. J.M. acknowledges support from the NASA through the NASA Hubble Fellowship grant HST-HF2-51414.001 awarded by the Space Telescope Science Institute, which is operated by the Association of Universities for Research in Astronomy, Inc., for NASA, under contract NAS5-26555. This work benefited from NASA's Nexus for Exoplanet System Science (NExSS) research coordination network, sponsored by NASA's Science Mission Directorate. Portions of this work were performed under the auspices of the U.S. Department of Energy by Lawrence Livermore National Laboratory under contract DE-AC52-07NA27344.

Facility: Gemini:South(GPI).

## ORCID iDs

Juan Sebastián Bruzzone  <https://orcid.org/0000-0002-2731-0397>  
 Stanimir Metchev  <https://orcid.org/0000-0003-3050-8203>  
 Gaspard Duchêne  <https://orcid.org/0000-0002-5092-6464>  
 Ruobing Dong  <https://orcid.org/0000-0001-9290-7846>  
 Thomas M. Esposito  <https://orcid.org/0000-0002-0792-3719>  
 Jason J. Wang  <https://orcid.org/0000-0003-0774-6502>  
 Johan Mazoyer  <https://orcid.org/0000-0002-9133-3091>  
 Schuyler Wolff  <https://orcid.org/0000-0002-9977-8255>  
 S. Mark Ammons  <https://orcid.org/0000-0001-5172-7902>  
 Adam C. Schneider  <https://orcid.org/0000-0002-6294-5937>

Alexandra Z. Greenbaum  <https://orcid.org/0000-0002-7162-8036>  
 Brenda C. Matthews  <https://orcid.org/0000-0003-3017-9577>  
 Pauline Arriaga  <https://orcid.org/0000-0001-6364-2834>  
 Vanessa P. Bailey  <https://orcid.org/0000-0002-5407-2806>  
 Travis Barman  <https://orcid.org/0000-0002-7129-3002>  
 Joanna Bulger  <https://orcid.org/0000-0003-4641-2003>  
 Jeffrey Chilcote  <https://orcid.org/0000-0001-6305-7272>  
 Tara Cotten  <https://orcid.org/0000-0003-0156-3019>  
 Robert J. De Rosa  <https://orcid.org/0000-0002-4918-0247>  
 Michael P. Fitzgerald  <https://orcid.org/0000-0002-0176-8973>  
 Katherine B. Follette  <https://orcid.org/0000-0002-7821-0695>  
 Benjamin L. Gerard  <https://orcid.org/0000-0003-3978-9195>  
 Stephen J. Goodsell  <https://orcid.org/0000-0002-4144-5116>  
 Pascale Hibon  <https://orcid.org/0000-0003-3726-5494>  
 Justin Hom  <https://orcid.org/0000-0001-9994-2142>  
 Li-Wei Hung  <https://orcid.org/0000-0003-1498-6088>  
 Patrick Ingraham  <https://orcid.org/0000-0003-3715-8138>  
 Quinn Konopacky  <https://orcid.org/0000-0002-9936-6285>  
 James E. Larkin  <https://orcid.org/0000-0001-7687-3965>  
 Bruce Macintosh  <https://orcid.org/0000-0003-1212-7538>  
 Franck Marchis  <https://orcid.org/0000-0001-7016-7277>  
 Christian Marois  <https://orcid.org/0000-0002-4164-4182>  
 Katie M. Morzinski  <https://orcid.org/0000-0002-1384-0063>  
 Eric L. Nielsen  <https://orcid.org/0000-0001-6975-9056>  
 Rebecca Oppenheimer  <https://orcid.org/0000-0001-7130-7681>  
 David Palmer  <https://orcid.org/0000-0001-7128-0802>  
 Rahul Patel  <https://orcid.org/0000-0002-5025-6827>  
 Marshall Perrin  <https://orcid.org/0000-0002-3191-8151>  
 Abhijith Rajan  <https://orcid.org/0000-0002-9246-5467>  
 Julien Rameau  <https://orcid.org/0000-0003-0029-0258>  
 Fredrik T. Rantakyro  <https://orcid.org/0000-0002-9667-2244>  
 Dmitry Savransky  <https://orcid.org/0000-0002-8711-7206>  
 Anand Sivaramakrishnan  <https://orcid.org/0000-0003-1251-4124>  
 Inseok Song  <https://orcid.org/0000-0002-5815-7372>  
 Remi Soummer  <https://orcid.org/0000-0003-2753-2819>  
 Sandrine Thomas  <https://orcid.org/0000-0002-9121-3436>  
 Kimberly Ward-Duong  <https://orcid.org/0000-0002-4479-8291>  
 Sloane Wiktorowicz  <https://orcid.org/0000-0003-4483-5037>

## References

- Augereau, J. C., Lagrange, A. M., Mouillet, D., & Ménard, F. 1999a, *A&A*, **350**, L51  
 Augereau, J. C., Lagrange, A. M., Mouillet, D., Papaloizou, J. C. B., & Grorod, P. A. 1999b, *A&A*, **348**, 557  
 Avenhaus, H., Quanz, S. P., Schmid, H. M., et al. 2014, *ApJ*, **781**, 87  
 Besla, G., & Wu, Y. 2007, *ApJ*, **655**, 528  
 Boccaletti, A., Thalmann, C., Lagrange, A.-M., et al. 2015, *Natur*, **526**, 230  
 Brittain, S. D., Rettig, T. W., Simon, T., et al. 2003, *ApJ*, **588**, 535  
 Burns, J. A., Lamy, P. L., & Soter, S. 1979, *Icar*, **40**, 1  
 Canovas, H., Ménard, F., de Boer, J., et al. 2015, *A&A*, **582**, L7  
 Clampin, M., Krist, J. E., Ardila, D. R., et al. 2003, *AJ*, **126**, 385  
 Currie, T., Grady, C. A., Cloutier, R., et al. 2016, *ApJL*, **819**, L26  
 Cutri, R. M., Skrutskie, M. F., van Dyk, S., et al. 2003, *yCat*, **2246**, 0  
 De Rosa, R. J., Nielsen, E. L., Blunt, S. C., et al. 2015, *ApJL*, **814**, L3  
 Dohnanyi, J. S. 1969, *JGR*, **74**, 2531  
 Dong, R., & Fung, J. 2017, *ApJ*, **835**, 38  
 Dong, R., Fung, J., & Chiang, E. 2016a, *ApJ*, **826**, 75  
 Dong, R., Hall, C., Rice, K., & Chiang, E. 2015a, *ApJL*, **812**, L32  
 Dong, R., Zhu, Z., Fung, J., et al. 2016b, *ApJL*, **816**, L12  
 Dong, R., Zhu, Z., Rafikov, R. R., & Stone, J. M. 2015b, *ApJL*, **809**, L5  
 Doucet, C., Pantin, E., Lagage, P. O., & Dullemond, C. P. 2006, *A&A*, **460**, 117  
 Fisher, R. S., Telesco, C. M., Piña, R. K., Knacke, R. F., & Wyatt, M. C. 2000, *ApJL*, **532**, L141  
 Flaherty, K. M., Hughes, A. M., Andrews, S. M., et al. 2016, *ApJ*, **818**, 97  
 Gaia Collaboration, Brown, A. G. A., Vallenari, A., et al. 2018, *A&A*, **616**, A1  
 Goto, M., Usuda, T., Dullemond, C. P., et al. 2006, *ApJ*, **652**, 758  
 Grady, C. A., Muto, T., Hashimoto, J., et al. 2013, *ApJ*, **762**, 48  
 Hashimoto, J., Tamura, M., Muto, T., et al. 2011, *ApJL*, **729**, L17  
 Hauschildt, P. H., Allard, F., & Baron, E. 1999, *ApJ*, **512**, 377  
 Høg, E., Fabricius, C., Makarov, V. V., et al. 2000, *A&A*, **355**, L27  
 Hughes, A. M., Wilner, D. J., Kamp, I., & Hogerheijde, M. R. 2008, *ApJ*, **681**, 626  
 Hung, L.-W., Bruzzone, S., Millar-Blanchaer, M. A., et al. 2016, *Proc. SPIE*, **9908**, 99083A  
 Jaschek, C., & Jaschek, M. 1992, *A&AS*, **95**, 535  
 Jaschek, M., Jaschek, C., & Egret, D. 1986, *A&A*, **158**, 325  
 Jonkheid, B., Kamp, I., Augereau, J.-C., & van Dishoeck, E. F. 2006, *A&A*, **453**, 163  
 Kalas, P., & Jewitt, D. 1995, *AJ*, **110**, 794  
 Klahr, H., & Lin, D. N. C. 2005, *ApJ*, **632**, 1113  
 Konishi, M., Grady, C. A., Schneider, G., et al. 2016, *ApJL*, **818**, L23  
 Kóspál, Á., Moór, A., Juhász, A., et al. 2013, *ApJ*, **776**, 77  
 Lagage, P. O., & Pantin, E. 1994, *Natur*, **369**, 628  
 Lagage, P. O., Pel, J. W., Authier, M., et al. 2004, *Msngr*, **117**, 12  
 Lagrange, A.-M., Bonnefoy, M., Chauvin, G., et al. 2010, *Sci*, **329**, 57  
 Li, A., & Lunine, J. I. 2003, *ApJ*, **594**, 987  
 Lyra, W., & Kuchner, M. 2013, *Natur*, **499**, 184  
 Macintosh, B., Graham, J. R., Ingraham, P., et al. 2014, *PNAS*, **111**, 12661  
 Maire, J., Ingraham, P. J., De Rosa, R. J., et al. 2014, *Proc. SPIE*, **9147**, 914785  
 Marois, C., Lafrenière, D., Doyon, R., Macintosh, B., & Nadeau, D. 2006, *ApJ*, **641**, 556  
 Marsh, K. A., Silverstone, M. D., Becklin, E. E., et al. 2002, *ApJ*, **573**, 425  
 Mawet, D., Choquet, É., Absil, O., et al. 2017, *AJ*, **153**, 44  
 Mazoyer, J., Boccaletti, A., Choquet, É., et al. 2016, *ApJ*, **818**, 150  
 Mendigutía, I., Mora, A., Montesinos, B., et al. 2012, *A&A*, **543**, A59  
 Merín, B., Montesinos, B., Eiroa, C., et al. 2004, *A&A*, **419**, 301  
 Millar-Blanchaer, M. A., Graham, J. R., Pueyo, L., et al. 2015, *ApJ*, **811**, 18  
 Milli, J., Vigan, A., Mouillet, D., et al. 2017, *A&A*, **599**, A108  
 Min, M., Rab, C., Woitke, P., Dominik, C., & Ménard, F. 2016, *A&A*, **585**, A13  
 Moór, A., Curé, M., Kóspál, Á., et al. 2017, *ApJ*, **849**, 123  
 Mouillet, D., Lagrange, A. M., Augereau, J. C., & Ménard, F. 2001, *A&A*, **372**, L61  
 Muto, T., Grady, C. A., Hashimoto, J., et al. 2012, *ApJL*, **748**, L22  
 Perrin, M. D., Duchene, G., Millar-Blanchaer, M., et al. 2015, *ApJ*, **799**, 182  
 Perrin, M. D., Maire, J., Ingraham, P., et al. 2014, *Proc. SPIE*, **9147**, 91473J  
 Perrot, C., Boccaletti, A., Pantin, E., et al. 2016, *A&A*, **590**, L7  
 Pinte, C., Harries, T. J., Min, M., et al. 2009, *A&A*, **498**, 967  
 Pinte, C., Ménard, F., Duchêne, G., & Bastien, P. 2006, *A&A*, **459**, 797  
 Pueyo, L., Soummer, R., Hoffmann, J., et al. 2015, *ApJ*, **803**, 31  
 Ressler, M. E., Werner, M. W., Van Cleve, J., & Chou, H. A. 1994, *ExA*, **3**, 277  
 Richert, A. J. W., Lyra, W., & Kuchner, M. J. 2018, *ApJ*, **856**, 41  
 Schmid, H. M., Joos, F., & Tschan, D. 2006, *A&A*, **452**, 657  
 Sloan, G. C., Keller, L. D., Forrest, W. J., et al. 2005, *ApJ*, **632**, 956  
 Soummer, R., Pueyo, L., & Larkin, J. 2012, *ApJL*, **755**, L28  
 Sylvester, R. J., Skinner, C. J., Barlow, M. J., & Mannings, V. 1996, *MNRAS*, **279**, 915  
 Thi, W.-F., Pinte, C., Pantin, E., et al. 2014, *A&A*, **561**, A50  
 van de Hulst, H. C. 1958, *QJRMS*, **84**, 198  
 Wagner, K., Apai, D., Kasper, M., & Roberto, M. 2015, *ApJL*, **813**, L2  
 Walker, H. J., & Wolstencroft, R. D. 1988, *PASP*, **100**, 1509  
 Wang, J. J., Rajan, A., Graham, J. R., et al. 2014, *Proc. SPIE*, **9147**, 914755  
 Wang, J. J., Ruffio, J.-B., De Rosa, R. J., et al. 2015, pyKLIP: PSF Subtraction for Exoplanets and Disks, Astrophysics Source Code Library, ascl:1506.001  
 Weinberger, A. J., Becklin, E. E., Schneider, G., et al. 1999, *ApJL*, **525**, L53  
 Weinberger, A. J., Rich, R. M., Becklin, E. E., Zuckerman, B., & Matthews, K. 2000, *ApJ*, **544**, 937  
 White, J. A., Boley, A. C., Hughes, A. M., et al. 2016, *ApJ*, **829**, 6  
 White, J. A., Boley, A. C., MacGregor, M. A., Hughes, A. M., & Wilner, D. J. 2018, *MNRAS*, **474**, 4500  
 Wyatt, M. C., Dermott, S. F., Telesco, C. M., et al. 1999, *ApJ*, **527**, 918  
 Zuckerman, B., Forveille, T., & Kastner, J. H. 1995, *Natur*, **373**, 494